VALLEYTRONICS

A valley valve and electron beam splitter

Jing Li[1]*, Rui-Xing Zhang[1], Zhenxi Yin[1], Jianxiao Zhang[1], Kenji Watanabe[2], Takashi Taniguchi[2], Chaoxing Liu[1], Jun Zhu[1,3]†

Developing alternative paradigms of electronics beyond silicon technology requires the exploration of fundamentally new physical mechanisms, such as the valley-specific phenomena in hexagonal two-dimensional materials. We realize ballistic valley Hall kink states in bilayer graphene and demonstrate gate-controlled current transmission in a four-kink router device. The operations of a waveguide, a valve, and a tunable electron beam splitter are demonstrated. The valley valve exploits the valley-momentum locking of the kink states and reaches an on/off ratio of 8 at zero magnetic field. A magnetic field enables a full-range tunable coherent beam splitter. These results pave a path to building a scalable, coherent quantum transportation network based on the kink states.

The advent of two-dimensional layered materials such as graphene and transition metal dichalcogenides has inspired the concept of devices that exploit the valley degrees of freedom in materials with hexagonal symmetry (*1*–*4*). Experiments have shown that a valley polarization can be created by current (*5*–*7*) or optical excitation (*8*). However, the realization of valleytronic devices remains challenging. In bilayer graphene, a perpendicular electric field applied through a pair of top and bottom gates breaks the symmetry of the two constituent layers and opens a gap Δ in its band structure (*9*, *10*). This gap can be inverted by switching the direction of the applied electric field; if two electric fields of opposite sign are applied on two neighboring regions in the sample, metallic, helical, quantum valley Hall kink states (hereafter kink states) emerge along the zero gap line (*11*). Topological in origin, the kink states are chiral in each valley and have opposite chiralities, that is, group velocities, in the two valleys K and K′ (−K) (Fig. 1A). They are expected to be immune from backscattering in the absence of valley-mixing scattering events and thus capable of carrying current ballistically over long distances without dissipation (*11*–*18*).

The intrinsic properties of the kink states enable several in situ transmission control mechanisms. Figure 1A illustrates the generation of kink states in bilayer graphene through asymmetric gapping (*11*, *12*). The shown chiralities correspond to the (− +) gating configuration. A (+ −) configuration simultaneously flips the chirality of the kink states in both valleys. Symmetric gapping configurations (+ +) or (− −) do not produce kink states and serve as controls in our experiment (fig. S3). The existence of two helicities produced by the (− +) and (+ −) gating is a unique attribute of the kink states and leads to the proposal of an all-electric valley valve (*12*, *14*), the operation of which relies on the valley-momentum locking of the kink states. Different from a classical spin valve (*19*), a valley polarization is not a requirement for the proposed valley valve. Here we show the realization of the valley valve with a transmission on/off ratio of 8 at zero magnetic field and greater than 100 at several teslas.

Figure 1, B to E, shows schematics and optical and scanning electron micrographs of the four-terminal valley router device, which consists of four pairs of split top and bottom gates and a global Si backgate (see fig. S1 for device fabrication). The aligned edges of the eight gates define the four kink channels shown in magenta in Fig. 1C. The dual-gated region (yellow areas in Fig. 1C) in each quadrant is gapped and placed at the charge neutrality point (CNP) (See fig. S2 for device characterization.) We first measure the resistance of each kink channel R_{kink} separately. As an example, Fig. 1G plots the resistance of the east channel R_E as a function of the Si backgate voltage V_{Si}, which controls the Fermi level E_F in the channel, at fixed magnetic fields B = 0 to 8 T. R_E exhibits a broad peak at B = 0, which evolves into a wide plateau as B increases and saturates at about 7.3 kilohm. This plateaued region corresponds to the gapped regime of the channel, where the kink states reside. We call this the kink regime. Its resistance value of 7.3 kilohm is a sum of the ballistic resistance of the kink states, that is, $h/4e^2$ = 6.5 kilohm, where h is the Planck constant, and a contact resistance R_c ~ 800 ohm. Additional plateaus outside the kink regime correspond to the sequential addition of fourfold degenerate quantum Hall edge states in the channel (Fig. 1F). The application of a perpendicular magnet field has little effect on the energy spectrum of the kink states (*11*, *20*) and does not generate additional edge states inside the bandgap [fig. S3; (*21*, *22*)]. It, however, turns the conduction and valence bands of the junction into Landau levels (Fig. 1F), as evidenced by the appearance of additional resistance plateaus. The devices studied here are of higher quality than those reported in our previous work (*11*), owing to the adoption of the van der Waals transfer method (*23*). A side effect of this approach, however, is a large width/length ratio of the dual-gated regions (Fig. 1D), which enhances parallel hopping conduction. At small magnetic fields, the associated resistance R_{para} causes R_E to be less than $h/4e^2$ (see curves for B = 0 and 2 T in Fig. 1G). We measure R_{para} independently using the symmetric gapping configurations (figs. S3 and S5) and extract R_E using a two-resistor model $R_E = \frac{(R_{24}-R_c)R_{para}}{R_{para}-(R_{24}-R_c)}$, where R_{24} is the resistance from terminal 2 to terminal 4. As B increases, hopping conduction becomes increasingly suppressed, and R_{para} grows to hundreds of megohms. R_{para} becomes inconsequential at 4 T, which leads to the observed saturation of $R_{24} = h/4e^2 + R_c$ in Fig. 1G. We determine R_c by fitting a series of quantized resistance plateaus and have observed robust resistance quantization of the kink states at $h/4e^2$ in different devices (fig. S4).

Similar measurements and analyses were performed on other channels in the same device and in a second device; the results are shown in Fig. 1H. At B = 0, R_{kink} is about 7000 ohm for our 300-nm-long channels, which corresponds to a transmission coefficient $\tau_{kink} = h/4e^2/R_{kink}$ = 0.92 and an estimated mean free path of 3.5 μm (*11*). This is on par with the mean free path of the quantum spin Hall edge states (*24*, *25*) and affirms the topological protection provided by the valley-momentum locking of the kink states. Because this protection vanishes in the armchair cryostallographic orientation, we ensure that neither of the two perpendicular directions of the channels is aligned with either zigzag or armchair orentations in our devices. Indeed, the similar performances of channels perpendicular to one another in our devices (Fig. 1H) support the existence of topological protection for both channels. The presence of a magnetic field improves the ballisticity of the kink states, which exhibit a quantized resistance plateau at B ~ 4 T. As discussed in our previous work (*11*), we suspect that the backscattering of the kink states is caused by one-dimensional nonchiral states bound in the junction, as well as by charge puddles inside the gap. The application of a magnetic field moves both types of states to higher energy, thus reducing their interactions with the kink states. Additionally, in the 0th Landau level of bilayer graphene, states in K and K′ occupy different graphene layers (*22*). If kink states behave similarly, this could contribute to reduced backscattering as well. A quantitative study can shed more light on this issue.

We now demonstrate the operation of the valley router as a reconfigurable waveguide for the kink states. Figure 2, A to C, shows three configurations of the waveguide, which we

[1]Department of Physics, The Pennsylvania State University, University Park, PA 16802, USA. [2]National Institute for Material Science, 1-1 Namiki, Tsukuba 305-0044, Japan. [3]Center for 2-Dimensional and Layered Materials, The Pennsylvania State University, University Park, PA 16802, USA.
*Present address: National High Magnetic Field Laboratory, Los Alamos, NM 87545, USA.
†Corresponding author. Email: jzhu@phys.psu.edu

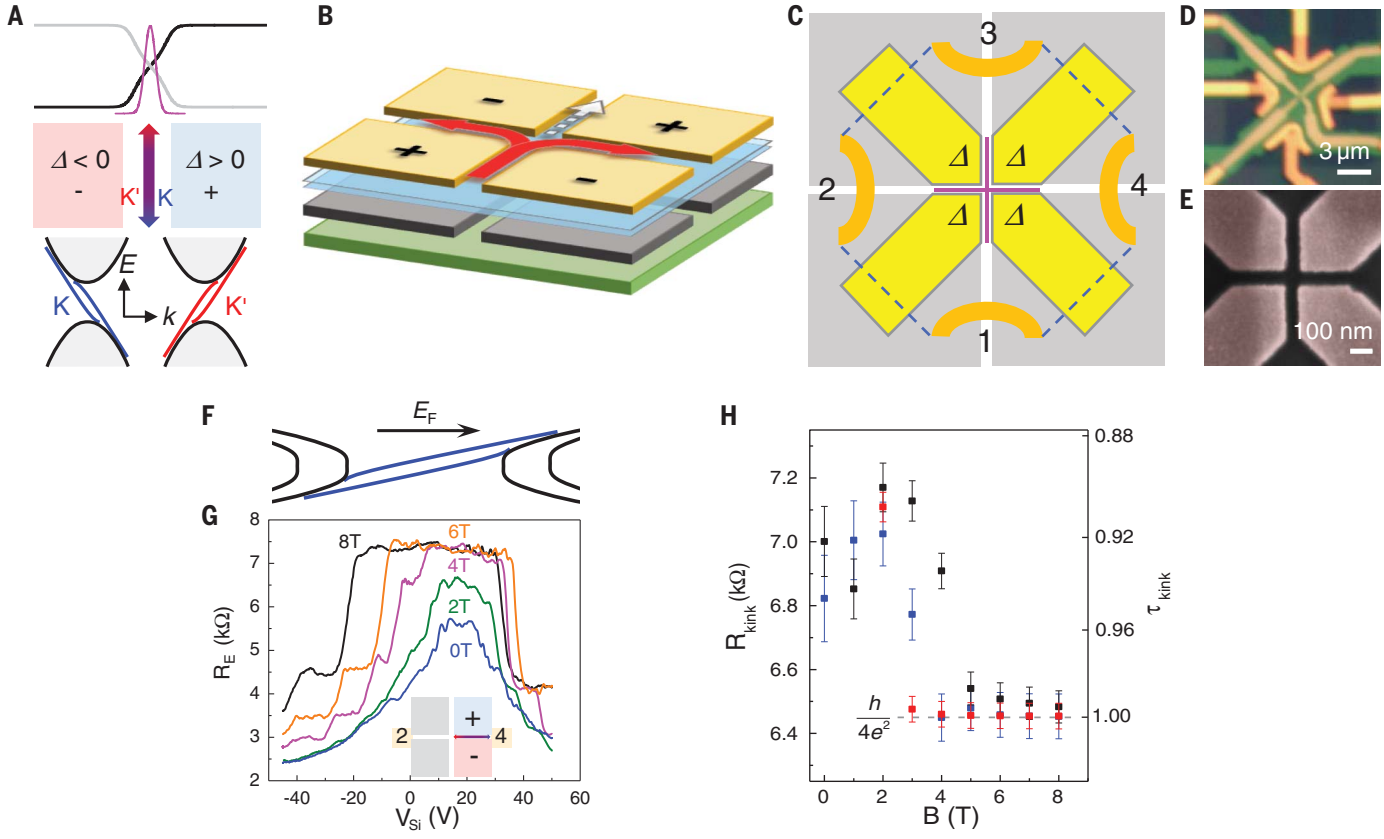

Fig. 1. A valley router device and ballistic conduction of the kink states. (**A**) The potential profile and wave function distribution (magenta curve) of the valley-momentum locked kink states in a 70-nm-wide junction (*11*). Including spin and layer isospin, there are four chiral modes in each valley. (**B** and **C**) Schematics of our quad-split-gated valley router device. The four graphite bottom gates are shown in gray. The four top gates are yellow. The bottom gates are set to ±3 V, with the polarity given in diagrams, unless otherwise specified. The top gates are set to place the dual-gated regions at the CNP. Three volts applied to the gates correspond to a bulk gap of Δ ~ 86 meV [see section 2 of (*27*)]. The blue sheet in (B) and dashed lines in (C) represent the bilayer graphene sheet. The global Si backgate is light green. The four gold arcs are Cr/Au side contacts. The magenta cross in (C) represents the four kink channels. Each is 70 nm wide and 300 nm long. The red arrows and white dashed arrow in (B) represent the valley valve and beam splitting actions discussed in Fig. 3. (**D**) An optical image of device 1. (**E**) A false-colored scanning electron micrograph of the central region taken on another device. (**F**) A band diagram of the junction in magnetic field (*11*). (**G**) R_E (V_{Si}) at different magnetic fields, as labeled in the graph. R_E is obtained by measuring R_{24}, that is, the resistance from terminal 2 to terminal 4, while doping the left quadrants heavily, as illustrated in the inset. (**H**) Resistance of the kink state R_{kink} as a function of the magnetic field in the east (black) and south (blue) channels of device 1 and south (red) channel of device 2. The right axis labels the corresponding transmission coefficient τ_{kink}. T = 1.6 K in all our measurements. Error bars indicate the uncertainties of R_{kink}.

label as "through," "right turn," and "left turn," respectively. In all three, the kink states only exist in two of the four channels, and the chirality in each valley is preserved along the paths. Figure 2D plots the measured through resistance R_{13}, together with the resistance of each individual kink channel R_N (north) and R_S (south) at 6 T. All three curves overlap in the kink regime, suggesting that the transmission through the intersection region is ballistic. Similar ballistic transmission is also observed in the two 90° bends (Fig. 2E), consistent with the results of numerical simulations (*14*, *26*). This four-terminal device thus serves as an in situ reconfigurable electronic waveguide of the kink states. The ability to go around a corner is a direct consequence of the topological nature of the kink states.

Deviation from perfect transmission starts to occur as the magnetic field B is lowered to B < 6 T. Figure 2F plots the transmission coefficient of the intersection region τ_i (B) determined using the two-resistor model shown as the inset (see fig. S5 for details). τ_i increases from 0.63 at B = 0 to unity at B ~ 6 T. τ_i is smaller than τ_{kink} of individual channels shown in Fig. 1H. This is not surprising because the confining bulk gaps in the intersection region are smaller and, consequently, nonchiral states may be present at lower energies to cause backscattering of the kink states (*11*). Increasing Δ—our device does not allow this owing to gate leakage—should enable further increase of τ_i toward unity. We discuss the current devices and improvements that can enable fully ballistic guiding of the kink states at B = 0 in section 2 of (*27*).

A more powerful operation of the valley router enables it to function as a valley valve and a coherent electron beam splitter simultaneously. In this operation, the polarity of the electric field changes sign between adjacent quadrants. Kink states in opposing channels have opposite helicities, that is, states with the same chirality carry opposite valley indices K and K′ and vice versa. This situation is depicted in the middle panel of Fig. 3A and leads to the suppression of straight current transmission in the absence of intervalley scattering. This valley-valve effect occurs regardless of the presence of a magnetic field and directly confirms the valley-momentum locking of the kink states. The application of a magnetic field, however, offers additional control of the wave function of the kink states. Calculations have shown that although the wave functions of the K and K′ valley kink states overlap at the CNP, where E_F = 0, they gradually shift in opposite directions as E_F moves into the electron or hole regime (*11*, *20*, *28*). The shifts are illustrated in the five panels of Fig. 3A. As the kink states shift away from the midlines of the channels, the wave function of a state coming from a particular channel has unequal overlap with states of adjacent channels, thus leading

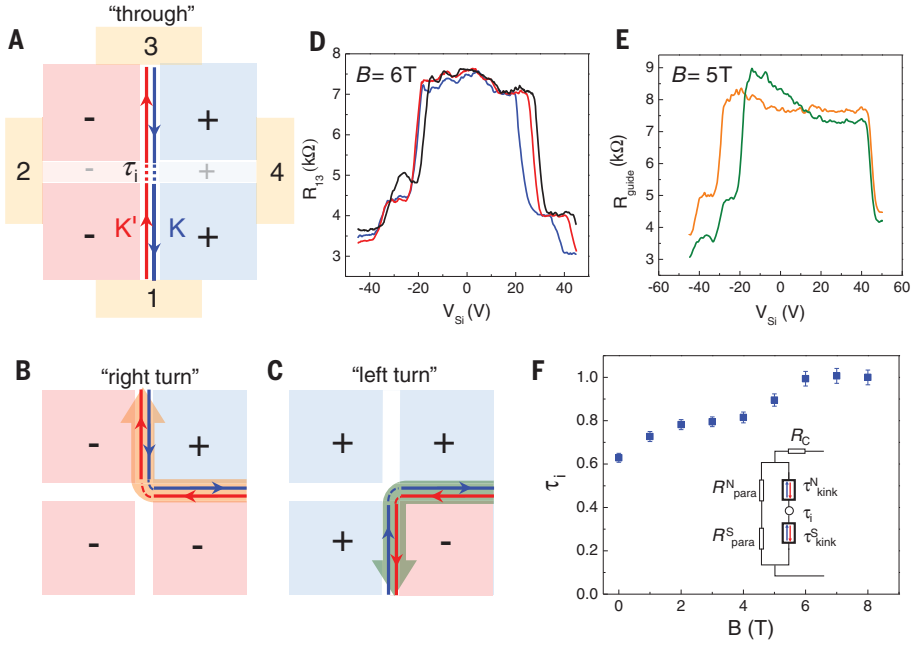

Fig. 2. Transmission of the kink states in the waveguide mode of the router. (**A** to **C**) Illustrations of the through (A), right turn (B), and left turn (C) configurations of the waveguide, respectively. (**D**) Two-terminal resistance R_{13} (V_{Si}) corresponding to the resistance of the north channel R_N (blue), the south channel R_S (red), and the through configuration (black). The overlap of all three indicates ballistic transmission through the intersection region in (A), that is, $\tau_i = 1$. $B = 6$ T. (**E**) R_{34} (orange) and R_{14} (green) as a function of V_{Si} in the configurations shown in (B) and (C), respectively. $B = 5$ T. (**F**) The transmission coefficient τ_i of the intersection region in (A) as a function of the magnetic field, with the schematic of the two-resistor model shown in the inset. Error bars indicate the uncertainties of τ_i.

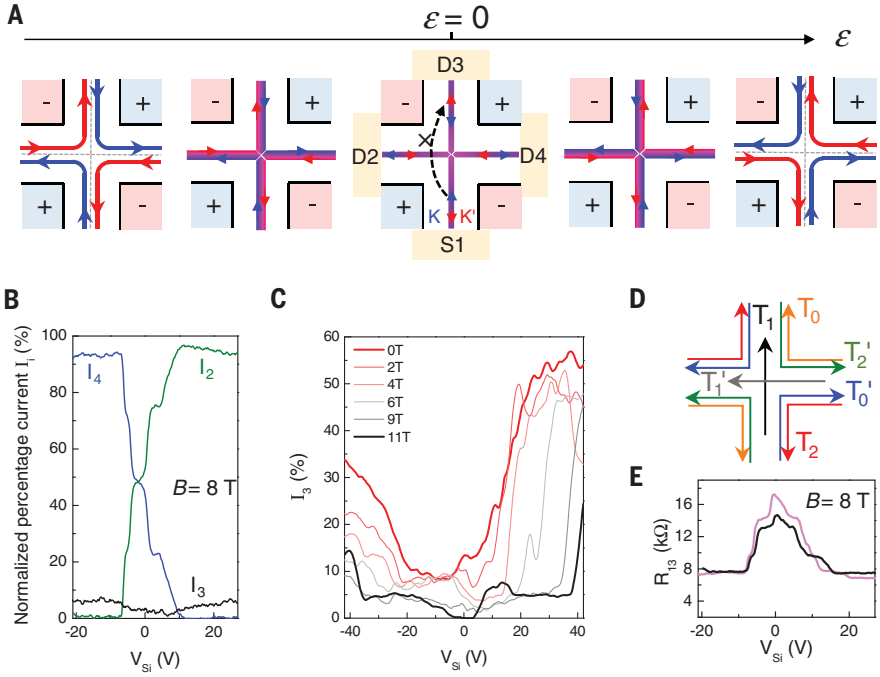

Fig. 3. A valley valve and electron beam splitter. (**A**) Evolution of the K and K′ kink state wave function center as a function of E_F in a moderate magnetic field. The arrows mark the chirality of the kink states, from the perspective of an electron. The middle panel represents the CNP, where the K and K′ states overlap. It also represents the $B = 0$ situation for all E_F. The dashed arrow illustrates the valley-valve blocking effect. (**B**) Measurements of the normalized percentage current I_i = [(current to drain i)/(total current)] ×100% received at terminals 2 to 4 as labeled in the graph while using terminal S1 as the current source. $B = 8$ T. The current flow is opposite of the arrows in (A). (**C**) I_3 (V_{Si}) at selected B fields from 0 to 11 T, demonstrating the robustness of the valley-valve effect. (**D**) The six independent current transmission coefficients used in our model (*27*), which reflects an empirical C_2 rotational symmetry of our device. (**E**) Measured (magenta) and calculated (black) two-terminal resistance R_{13}. A contact resistance $R_c = 1$ kilohm is added to the calculated curve. $B = 8$ T. The discrepancy between theory and experiment may be caused by local microscopic imperfections of the device beyond the S-matrix model.

to unequal current partition. Simulations show that the wave function separation is tunable as a function of E_F and B and can become comparable to or greater than the width of the wave functions themselves at several teslas (*11*, *28*). Consequently, a current partition from 0 to 1 is possible.

To test these predictions experimentally, we source a constant current from one terminal and measure the normalized percentage current I_i = [(current to drain i)/(total current)] × 100% received at the other three terminals simultaneously. Figure 3B plots I_2, I_3, and I_4 at $B = 8$ T using S1 labeled in Fig. 3A as the current source. Notably, I_3 remains low in the entire range of V_{Si} when all four channels are in the kink regime. Similar behavior is observed in measurements using other source terminals (fig. S7) and in device 2 (fig. S8). The suppression of current flow between opposing terminals provides compelling evidence of the valley-valve effect, which also confirms the valley-momentum locking of the kink states. As Fig. 3C shows, the valley-valve effect is already very strong at $B = 0$, with a small I_3 of 8% near the CNP. I_3 further decreases to less than 1% at $B = 11$ T, as the magnetic field works to suppress residual intervalley scattering in the intersection region. The transmission on/off ratio of I_3 between the through configuration (Fig. 2A) and the blocking configuration

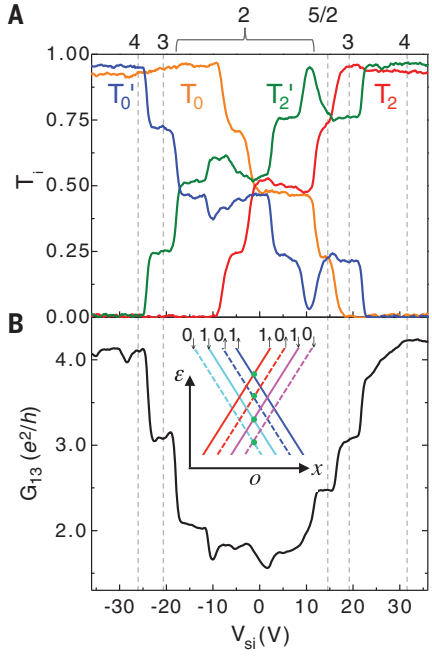

Fig. 4. Quantized transmission coefficients in a strong magnetic field. (**A** and **B**) Measured transmission coefficients T_0, T_2, T_0', and T_2' (A) and G_{13} (B) as a function of V_{Si} at B = 16 T. The locations of the quantized G_{13} are marked in the plot; their conductance values are labeled at the top axis in units of e^2/h. Spikes in the middle of a plateau are likely caused by microscopic potential irregularities. A contact resistance of R_c = 1174 ohm is subtracted. The inset of (B) shows a guiding center description of the energy spectrum of the valley kink states in strong magnetic and electric fields.

(Fig. 3A) is about 8 at B = 0 and greater than 100 in a magnetic field. The performance of the valley valve is similar to a recently reported state-of-the-art all-electric spin valve (*29*). Unlike a spin valve, however, here the source current is nearly valley-unpolarized. The omission of the valley injection step is an advantage of the underlying topological valleytronic concept.

Instead of propagating forward, the kink state wave functions from S1 split at the intersection and propagate toward terminals D2 and D4. Both I_2 and I_4 vary colinearly with V_{Si}, forming a prominent X-like feature at 8 T (Fig. 3B). The tunable range of I_2 (I_4) increases with B until it saturates close to the full range of 0 to 1 at ~5 T (fig. S7, A and B). This current partition behavior is reproducible using different source terminals (fig. S7C) and in different devices (fig. S8). It is in excellent agreement with the wave function separation scenarios depicted in Fig. 3A and represents an electron analog of an optical beam splitter and a quantum point contact for the kink states. Furthermore, in fig. S7D, we show the large impact of unequal gap size on the current partition. By adjusting the size of the gap on the four quadrants at a fixed E_F, I_2 (I_4) can change by 50%. These results are promising steps toward the implementation of a zero-magnetic field beam splitter (*28*).

We developed an S-matrix model [section 8 of (*27*)] to describe the transmissions of the kink states between different channels with six independent coefficients schematically shown in Fig. 3D. These coefficients are obtained directly from measurements shown in Fig. 3B and in other source-drain setups (fig. S7). Using the experimental input and the Landauer-Büttiker formula, we have calculated the resistance for various two-terminal and nonlocal measurement geometries and compared them to measurements. The agreement between theory and experiment is excellent and affirms the one-dimensional transport nature of the kink states. As an example, Fig. 3E shows the calculated and measured two-terminal resistance R_{13}; other scenarios are discussed in fig. S10. More fundamental understandings and predictions of the transmission process would require details of the electrostatics (*28*) and also possibly band-structure effects such as trigonal wrapping (*30*, *31*).

When the magnetic field increases to above 6 T, plateaus at ¼, ½, and ¾ start to appear in the transmission coefficient T_i. Correspondingly, conductance plateaus in integer and half-integer units of e^2/h appear in the measured conductance between terminals 1 and 3 G_{13}. The quantization becomes increasingly prominent and precise as B increases, with the data of T_i and G_{13} at B = 16 T given in Fig. 4, A and B. (See fig. S11 for data up to 18 T.) Their appearance is caused by the energy splitting of the four kink-state modes in a strong magnetic field (inset of Fig. 4B) (*32*) and, consequently, the spatial separation of the modes in a guiding center description. The large spatial separation between the modes leads to values of T_i taking either 0 or 1 for each mode, with the choice given by the position of E_F with respect to the crossing point of that mode. The average of all four modes then produces quantized coefficients at multiples of ¼. This leads to conductance plateaus quantized in integer and half integer units of e^2/h, as Fig. 4B shows. In section 9 of (*27*), we provide a detailed understanding of the fractional quantization of T_i and its manifestation in transport, which reflect the coexisting helical and chiral nature of the kink states in a magnetic field.

REFERENCES AND NOTES

1. A. Rycerz, J. Tworzydlo, C. W. J. Beenakker, *Nat. Phys.* **3**, 172–175 (2007).
2. W. Yao, D. Xiao, Q. Niu, *Phys. Rev. B* **77**, 235406 (2008).
3. D. Xiao, M.-C. Chang, Q. Niu, *Rev. Mod. Phys.* **82**, 1959–2007 (2010).
4. X. Xu, W. Yao, D. Xiao, T. F. Heinz, *Nat. Phys.* **10**, 343–350 (2014).
5. R. V. Gorbachev *et al.*, *Science* **346**, 448–451 (2014).
6. Y. Shimazaki *et al.*, *Nat. Phys.* **11**, 1032–1036 (2015).
7. M. Sui *et al.*, *Nat. Phys.* **11**, 1027–1031 (2015).
8. K. F. Mak, K. L. McGill, J. Park, P. L. McEuen, *Science* **344**, 1489–1492 (2014).
9. Y. Zhang *et al.*, *Nature* **459**, 820–823 (2009).
10. E. McCann, M. Koshino, *Rep. Prog. Phys.* **76**, 056503 (2013).
11. J. Li *et al.*, *Nat. Nanotechnol.* **11**, 1060–1065 (2016).
12. I. Martin, Y. M. Blanter, A. F. Morpurgo, *Phys. Rev. Lett.* **100**, 036804 (2008).
13. J. Li, A. F. Morpurgo, M. Büttiker, I. Martin, *Phys. Rev. B* **82**, 245404 (2010).
14. Z. Qiao, J. Jung, Q. Niu, A. H. Macdonald, *Nano Lett.* **11**, 3453–3459 (2011).
15. J. Jung, F. Zhang, Z. Qiao, A. H. MacDonald, *Phys. Rev. B* **84**, 075418 (2011).
16. F. Zhang, A. H. MacDonald, E. J. Mele, *Proc. Natl. Acad. Sci. U.S.A.* **110**, 10546–10551 (2013).
17. L. Ju *et al.*, *Nature* **520**, 650–655 (2015).
18. J. Lee, K. Watanabe, T. Taniguchi, H. J. Lee, *Sci. Rep.* **7**, 6466 (2017).
19. S. Datta, B. Das, *Appl. Phys. Lett.* **56**, 665–667 (1990).
20. M. Zarenia, J. M. Pereira Jr., G. A. Farias, F. M. Peeters, *Phys. Rev. B* **84**, 125451 (2011).
21. E. McCann, V. I. Fal'ko, *Phys. Rev. Lett.* **96**, 086805 (2006).
22. J. Li, Y. Tupikov, K. Watanabe, T. Taniguchi, J. Zhu, *Phys. Rev. Lett.* **120**, 047701 (2018).
23. L. Wang *et al.*, *Science* **342**, 614–617 (2013).
24. M. König *et al.*, *Science* **318**, 766–770 (2007).
25. L. Du, I. Knez, G. Sullivan, R.-R. Du, *Phys. Rev. Lett.* **114**, 096802 (2015).
26. Z. Qiao *et al.*, *Phys. Rev. Lett.* **112**, 206601 (2014).
27. See supplementary materials.
28. K. Wang *et al.*, *Phys. Rev. B* **95**, 245420 (2017).
29. P. Chuang *et al.*, *Nat. Nanotechnol.* **10**, 35–39 (2015).
30. D. A. Cosma, V. I. Fal'ko, *Phys. Rev. B* **92**, 165412 (2015).
31. A. Varlet *et al.*, *Phys. Rev. Lett.* **113**, 116602 (2014).
32. M. Victoria, S. Efrat, H. Chia-Wei, T. C. Sam, H. A. Fertig, *Phys. Scr. T* **165**, 014019 (2015).
33. J. Li, Data for "A valley valve and electron beam splitter," Version 1, Harvard Dataverse (2018); https://doi.org/10.7910/DVN/UIFTE6.

ACKNOWLEDGMENTS

We are grateful for helpful discussions with J. Teo. We thank J. Jaroszynski of the NHMFL for experimental assistance. **Funding:** J.L., Z.Y., and J.Zhu are supported by the NSF (grant no. DMR-1506212 and DMR-1708972). C.L., J.Zha., and R.-X.Z. acknowledge support from the Office of Naval Research (grant nos. N00014-15-1-2675). K.W. and T.T. acknowledge support from the Elemental Strategy Initiative conducted by the MEXT, Japan, and the CREST (JPMJCR15F3), JST. Part of this work was performed at the NHMFL, which was supported by the NSF through NSF-DMR-1157490 and the state of Florida. Part of this work was carried out in the Nanofabrication Laboratory at Penn State's Materials Research Institute. **Author contributions:** J.Zhu and J.L. conceived the experiment. J.L. designed and fabricated the devices and made the measurements. Z.Y. assisted in device fabrications. J.L. and J.Zhu analyzed the data. R.-X.Z. and J.Zha. performed the theoretical calculations. R.-X.Z. and C.L. analyzed theoretical results. K.W. and T.T. synthesized the hexagonal boron nitride crystals. J.Zhu, J.L., R.-X.Z., and C.L. wrote the manuscript with input from all authors. **Competing financial interests:** The authors declare no competing financial interests. **Data and materials availability:** Data shown in this paper are available at (*33*).

SUPPLEMENTARY MATERIALS

www.sciencemag.org/content/362/6419/1149/suppl/DC1
Supplementary Text
Figs. S1 to S14
Table S1
References (*34*–*36*)

7 August 2017; resubmitted 28 March 2018
Accepted 30 October 2018
10.1126/science.aao5989

A valley valve and electron beam splitter

Jing Li, Rui-Xing Zhang, Zhenxi Yin, Jianxiao Zhang, Kenji Watanabe, Takashi Taniguchi, Chaoxing Liu and Jun Zhu

Science **362** (6419), 1149-1152.
DOI: 10.1126/science.aao5989

Making a practical valleytronics device

Two-dimensional materials with a hexagonal lattice, such as graphene, have two distinct "valleys" in their band structure. Researchers in the emerging field of valleytronics hope that these valley degrees of freedom can be exploited as information carriers, but making valleytronic devices is tricky. Li *et al.* created chiral valley Hall states on the boundary between oppositely gated regions of bilayer graphene. They then guided these so-called kink states through their sample using spatially modulated gating, demonstrating right and left turns, as well as a valley valve function.

Science, this issue p. 1149